

Spin-torque excitation of perpendicular standing spin waves in coupled YIG/Co heterostructures

Stefan Klingler,^{1,2,*} Vivek Amin,^{3,4} Stephan Geprägs,^{1,2} Kathrin Ganzhorn,^{1,2} Hannes Maier-Flaig,^{1,2} Matthias Althammer,^{1,2} Hans Huebl,^{1,2,5} Rudolf Gross,^{1,2,5} Robert D. McMichael,³ Mark D. Stiles,³ Sebastian T.B. Goennenwein,^{6,7} and Mathias Weiler^{1,2}

¹*Walther-Meißner-Institut, Bayerische Akademie der Wissenschaften, 85748 Garching, Germany*

²*Physik-Department, Technische Universität München, 85748 Garching, Germany*

³*Center for Nanoscale Science and Technology, National Institute of Standards and Technology, Gaithersburg, Maryland 20899-6202, USA*

⁴*Institute for Research in Electronics and Applied Physics, University of Maryland, College Park, MD 20742*

⁵*Nanosystems Initiative Munich, 80799 Munich, Germany*

⁶*Institut für Festkörperphysik, Technische Universität Dresden, 01062 Dresden, Germany*

⁷*Center for Transport and Devices of Emergent Materials, Technische Universität Dresden, 01062 Dresden, Germany*

We investigate yttrium iron garnet (YIG)/cobalt (Co) heterostructures using broadband ferromagnetic resonance (FMR). We observe an efficient excitation of perpendicular standing spin waves (PSSWs) in the YIG layer when the resonance frequencies of the YIG PSSWs and the Co FMR line coincide. Avoided crossings of YIG PSSWs and the Co FMR line are found and modeled using mutual spin pumping and exchange torques. The excitation of PSSWs is suppressed by a thin aluminum oxide (AlOx) interlayer but persists with a copper (Cu) interlayer, in agreement with the proposed model.

In magnonics, information is encoded into the electron spin-angular momentum instead of the electron charge used in conventional complementary metal-oxide semiconductor (CMOS) technology [1–10]. Magnonics based on exchange spin waves is particularly appealing, due to isotropic spin-wave propagation with small wavelengths and large group velocities [5]. With its long magnon propagation length, yttrium iron garnet (YIG) is especially interesting for this application. However, an excitation of exchange spin waves by microwave magnetic fields requires nanolithographically defined microwave antennas [11] that have poor efficiency due to high ohmic losses and impedance mismatch.

Here, we show that exchange spin waves can be excited by interfacial spin torques (ST) in YIG/Co heterostructures. These STs couple the YIG and Co magnetization dynamics by microwave frequency spin currents [12]. Phenomenological modeling of the coupling reveals a combined action of exchange, damping-like and field-like torques that are localized at the YIG/Co interface. This is in contrast to the previously observed purely damping-like ST in all-metallic multilayers [13].

We study the magnetization dynamics of YIG/Co thin film heterostructures by broadband ferromagnetic resonance (FMR) spectroscopy. From our FMR data we find an efficient excitation of perpendicular standing spin waves (PSSWs) in the YIG when the YIG PSSW resonance frequency is close to the Co FMR line. We observe about 40 different PSSWs with wavelengths down to $\lambda_{\text{PSSW}} \approx 50$ nm.

Clear evidence for the coupling is provided by avoided crossings and corresponding characteristic changes of the linewidths of the YIG PSSW and the Co FMR line. This coupling and the excitation of PSSWs is also observed when a copper (Cu) layer separates the YIG and the Co films. However, the insertion of an insulating AlOx interlayer completely suppresses the excitation of YIG PSSWs. This allows us to exclude dipolar coupling as the origin of the PSSW excitation and is in agreement with the mediation of the coupling by spin currents. Our data are well described by a modified Landau-Lifshitz-Gilbert equation for the Co layer, which includes direct exchange torques and spin torques from mutual spin pumping at the YIG/Co interface. Simulations of our coupled systems reveal the strong influence of spin currents on the coupling of the different layers.

We investigate a set of four YIG/Co samples, which are YIG/Co(50), YIG/Co(35), YIG/Cu(5)/Co(50) and YIG/AlOx(1.5)/Co(50), where the numbers in brackets denote the layer thicknesses in nanometers. The YIG thickness d_2 is $= 1 \mu\text{m}$ for all samples. The FMR measurements are performed at room temperature using a coplanar waveguide (CPW) with a center conductor width of $w = 300 \mu\text{m}$. The CPW is connected to the two ports of a vector network analyzer (VNA) and we measure the complex S_{21} parameter as a function of frequency f and external magnetic field H for a fixed microwave power of 1 mW (0 dBm) [14], well below the threshold for any non-linear effects (for details of the sample preparation and the FMR setup see Supplemental Material S1 and S2 [15]).

Fig. 1(a) shows the background-corrected field-derivative [16] of the VNA transmission spectra $|\partial_{\text{D}} S_{21} / \partial H|$ for the YIG/Co(50) sample as a function

* stefan.klingler@wmi.badw.de

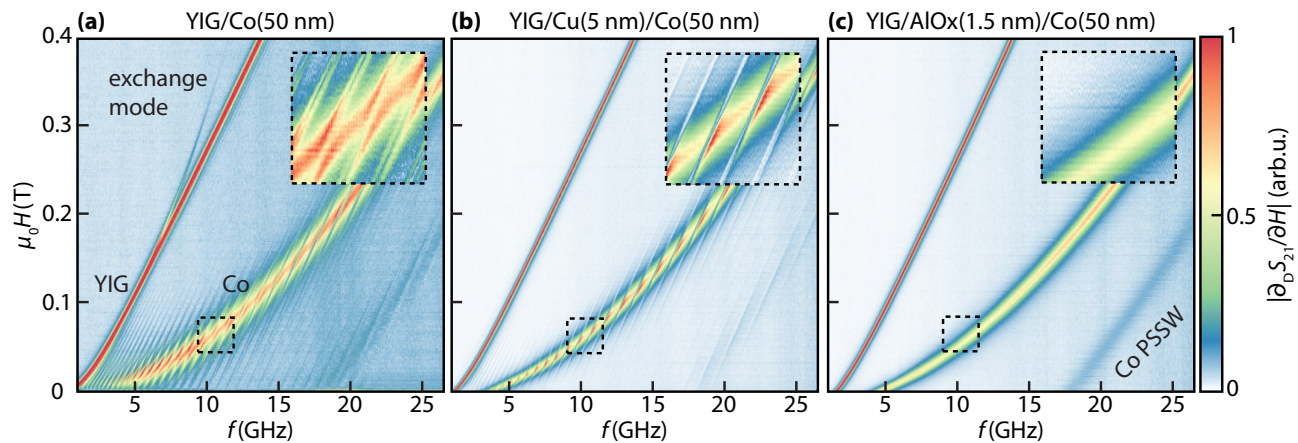


FIG. 1. (Color online) Field-derivative of the Vector Network Analyzer (VNA) transmission spectra for three different samples as a function of magnetic field and frequency. All samples show two modes corresponding to the YIG (low-frequency mode) and Co (high-frequency mode) FMR lines. The color scale is individually normalized to arbitrary values. (a) The YIG/Co(50) sample additionally reveals YIG PSSWs and pronounced avoided crossings of the modes for small frequencies. (b) The YIG/Cu(5)/Co(50) sample also shows the YIG PSSWs, but the frequency splittings of the modes are much smaller than in (a). (c) The YIG/AlOx(1.5)/Co(50) sample does not show any PSSWs in the Co FMR line as expected if the YIG and the Co films are magnetically uncoupled.

of H and f as explained in S3 [15] and we clearly observe two major modes. The low frequency mode corresponds to the YIG FMR line, whereas the high-frequency mode corresponds to the Co FMR line. Within the broad Co FMR line, we find several narrow resonances, of which the dispersion is parallel to the YIG FMR. These lines are attributed to the excitation and detection of YIG PSSWs with wavelengths down to 50 nm (for details see Fig. S5 [15]). We find avoided crossings between these YIG PSSWs and the Co FMR line (inset), where the frequency splitting $g_{\text{eff}}/2\pi \leq 200$ MHz (see S4 [15] for details). This is a clear indication that the YIG and Co modes are coupled to each other. Furthermore, an additional low-frequency mode with lower intensity is observed in Fig. 1(a). This line is attributed to an exchange mode of the coupled YIG/Co system. This is in agreement with previous observations of exchange modes in coupled systems [17–19]. A qualitatively similar transmission spectrum is observed for the YIG/Co(35) sample (for details see Fig. S6 [15]). Furthermore, we observe the first Co PSSW at around $f = 22$ GHz and $\mu_0 H = 0.1$ T for samples with a 50 nm thick Co layer.

Fig. 1(b) shows $|\partial_D S_{21}/\partial H|$ for the YIG/Cu(5)/Co(50) sample as a function of H and f . Again, we observe the YIG FMR, YIG PSSWs and the Co FMR lines. However, the frequency splitting between the modes (inset) is much smaller in comparison to the YIG/Co(50) sample, $g_{\text{eff}}/2\pi \leq 40$ MHz. This strongly indicates that the coupling efficiency is reduced in comparison to Fig. 1(a). We attribute this mainly to the suppression of the static exchange coupling by insertion of the Cu layer. This is also in agreement with the vanishing of the exchange mode, as previously observed in [18] for Ru interlayers

with thickness > 2 nm. Fig. 1(c) displays $|\partial_D S_{21}/\partial H|$ for the YIG/AlOx(1.5)/Co(50) sample as a function of H and f . No YIG PSSWs are observed within the Co FMR line (inset Fig. 1(c)). This provides strong evidence that the insertion of the thin AlOx layer suppresses the coupling between the YIG and Co magnetization dynamics. An analysis of the Co FMR linewidth (for details see S7 [15]) also demonstrates that the AlOx layer eliminates any coupling between the YIG and Co layers. From Fig. 1, we conclude that any magneto-dynamic coupling is suppressed by insertion of a thin insulator between the two magnetic layers. This provides strong evidence against a magnetostatic coupling by stray fields, and is in agreement with a dynamic coupling mediated by spin currents, which can pass through the Cu layer, but are blocked by the AlOx barrier.

Fig. 2 shows the magnetic hysteresis loops of the YIG/Co samples recorded by Superconducting Quantum Interference Device (SQUID) magnetometry. The hysteresis loop of the YIG/Co(50) sample (solid blue line in Fig. 2) exhibits a sharp switching at the YIG coercive field of about 0.1 mT. However, no sharp switching of the Co layer is visible but a smooth increase of the measured magnetic moment until the bilayer magnetization is saturated. This can be explained by a direct, static exchange coupling between YIG and Co magnetizations (inset), as known from exchange springs [20, 21]. The form of the hysteresis loop suggests an antiferromagnetic coupling, as comparably large magnetic fields are required to force a parallel alignment of the layers. However, without a detailed examination of the remnant state, we cannot rule out any ferromagnetic coupling. By inserting a Cu or AlOx layer between the YIG and the Co (dash-dotted and

dashed lines in Fig. 2) we find a sharp switching at the Co coercive field $\mu_0 H_c \approx 1$ mT. This switching is in agreement with the notion, that the 5 nm-thick Cu interlayer and the insulating AlOx interlayer suppress any exchange coupling between the YIG and the Co [22]. Small differences of the Co coercive field in the YIG/Cu/Co and YIG/AlOx/Co in Fig. 2 are attributed to different roughnesses of the underlying Cu and AlOx layers. However, we still observe a dynamic coupling in Fig. 1 (b) in the YIG/Cu(5)/Co(50) sample. Since we expect no static exchange coupling between Co and YIG in this sample, this observation requires a different mechanism for the origin of the excitation of the YIG PSSWs.

We model the data of Fig. 1 with a modified Landau-Lifshitz-Gilbert approach, which includes finite mode coupling between the YIG and the Co magnetizations at the YIG/Co interface at $z = d_2$. We model the Co magnetization \mathbf{M}_1 as a macrospin, which is fixed primarily along the y -direction with small transverse parts and the YIG magnetization $\mathbf{M}_2(z)$ as a vector that depends on the distance z from the YIG/Co interface (for detailed calculations see S8, S9 [15]). In the limit that the transverse parts are small, the equation of motion for the Co

macrospin then reads:

$$\begin{aligned} \dot{\mathbf{M}}_1 = & -\gamma_1 \hat{\mathbf{y}} \times \left[-\mu_0 H \mathbf{M}_1 - \frac{\alpha_1}{\gamma_1} \dot{\mathbf{M}}_1 - \mu_0 M_{s,1} M_{1,z} \hat{\mathbf{z}} \right. \\ & \left. - \frac{J}{d_1 M_{s,1}} (\mathbf{M}_1 - \mathbf{M}_2(d_2)) - \mu_0 \mathbf{h} \right] \\ & - \frac{\gamma_1}{d_1 M_{s,1}} [(\tau_F - \tau_D \hat{\mathbf{y}} \times) (\dot{\mathbf{M}}_1 - \dot{\mathbf{M}}_2(d_2))]. \end{aligned} \quad (1)$$

Here, α_1 is the Gilbert damping parameter for Co, γ_1 and $M_{s,1}$ its gyromagnetic ratio and saturation magnetization, respectively, $\hat{\mathbf{z}}$ is the unit vector in z -direction, and d_1 is the thickness of the Co layer. The magnetic driving field from the CPW is denoted by \mathbf{h} . In our model, \mathbf{h} is assumed to be spatially uniform, to reflect the experimental situation where the CPW center conductor width is much larger than either the YIG or Co thickness. The exchange coupling constant between the YIG and the Co is given by J . The torques due to spin currents pumped from one layer and absorbed in the other have field-like τ_F and damping-like τ_D components. The YIG magnetization direction at the YIG/Co interface is given by $\mathbf{M}_2(d_2)$. The YIG magnetization obeys two boundary conditions [23–25]. First, the total torque on the YIG/Co interface at $z = d_2$ has to vanish:

$$\begin{aligned} 0 = & 2A \hat{\mathbf{y}} \times \partial_z \mathbf{M}_2(z)|_{z=d_2} - J \hat{\mathbf{y}} \times (\mathbf{M}_1 - \mathbf{M}_2(d_2)) \\ & + (\hbar/e)(\tau_F - \tau_D \hat{\mathbf{y}} \times) (\dot{\mathbf{M}}_1 - \dot{\mathbf{M}}_2(d_2)). \end{aligned} \quad (2)$$

Here, A is the exchange constant of YIG. Second, we assume an uncoupled boundary condition at the YIG/substrate interface

$$0 = 2A \hat{\mathbf{y}} \times \partial_z \mathbf{M}_2(z)|_{z=0}, \quad (3)$$

where the torque vanishes as well. The Co susceptibility χ_1 is then derived using the ansatz for the transverse YIG magnetization $\mathbf{m}_2(z, t) = (m_{2,x}(z, t), m_{2,z}(z, t))$:

$$\begin{aligned} \mathbf{m}_2(z, t) = & \text{Re} [c_+ \mathbf{m}_{2+} \cos(kz) \exp(-i\omega t) + \\ & c_- \mathbf{m}_{2-} \cos(\kappa z) \exp(-i\omega t)]. \end{aligned} \quad (4)$$

Here, $\mathbf{m}_{2\pm}$ are the complex eigenvectors of the uncoupled transverse YIG magnetization, c_{\pm} are complex coefficients, $\omega = 2\pi f$ is the angular frequency, k and κ are complex wavevectors of the undisturbed YIG films. The transverse Co magnetization follows a simple elliptical precession:

$$\mathbf{m}_1 = \text{Re} [\mathbf{m}_{1,0} \exp(-i\omega t)] \quad (5)$$

where $\mathbf{m}_1 = (m_{1,x}, m_{1,z})$, and $\mathbf{m}_{1,0} \approx (m_{1,0,x}, m_{1,0,z})$ is a complex precession amplitude. After finding the complex coefficients c_{\pm} , the Co susceptibility χ_1 can be obtained from Eq. (1).

Fig. 3 (a-c) show the simulated microwave signal $|\partial_D S_{21}/\partial H| \propto |\partial \chi_1/\partial H|$ (for details see S3, S9 [15]). For all simulations we take the same material parameters, namely $\mu_0 M_{s,1} = 1.91$ T, $A = 3.76$ pJ/m, $\alpha_1 = 7.7 \times 10^{-3}$,

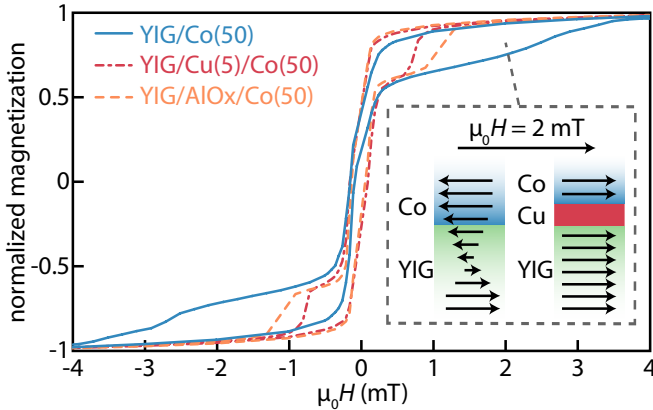


FIG. 2. Magnetization of YIG/Co(50) (solid), YIG/Cu(5)/Co(50) (dash-dotted) and YIG/AlOx(1.5)/Co(50) (dashed) normalized to the magnetization at $\mu_0 H = 4$ mT. The magnetic hysteresis loops of YIG/Co show an enhancement of the Co coercive field as well as a rather smooth switching. The samples with a Cu or AlOx interlayer reveal a sharp switching of the magnetization at the Co coercive field $\mu_0 H_c \approx 1$ mT. The inset shows a possible static magnetization distribution in an exchange coupled (left) and an uncoupled (right) heterostructure at an external magnetic field of $\mu_0 H = 2$ mT. In the latter case, both static magnetizations are independently aligned parallel to the external field direction, as the external field amplitude exceeds the coercive fields of YIG and Co.

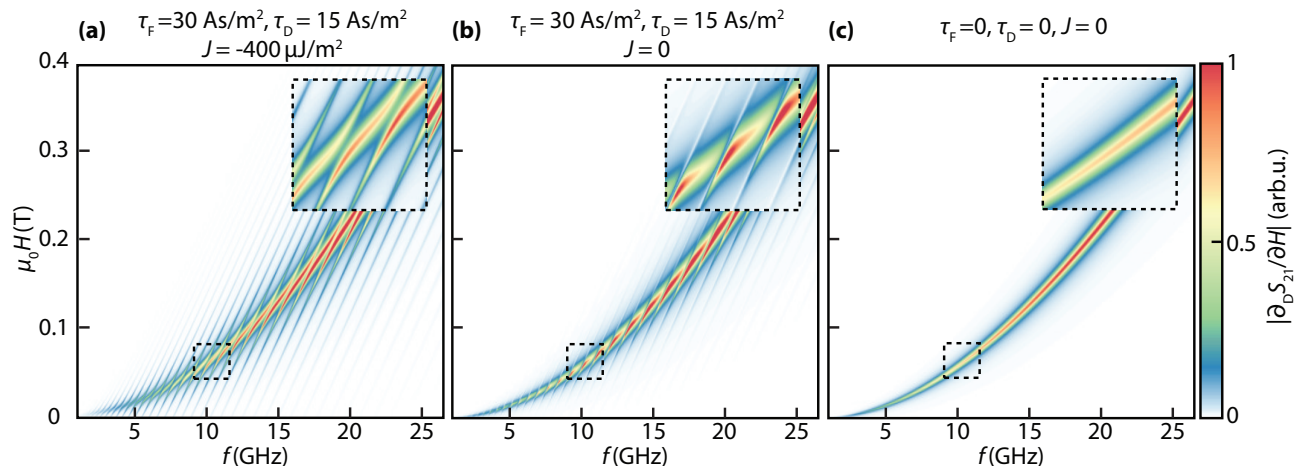


FIG. 3. (Color online) Calculated $|\partial_D S_{21}/\partial H|$ of the simulated transmission spectra. Simulation of the (a) YIG/Co(50) sample, (b) YIG/Cu(5)/Co(50) sample, (c) YIG/AlOx(1.5)/Co(50) sample.

$\alpha_2 = 7.2 \times 10^{-4}$, $\gamma_1 = 28.7$ GHz/T and $\gamma_2 = 27.07$ GHz/T, as extracted in S4, S5, S7 [15], which are in good agreement with previous reports [26–29]. The thicknesses are $d_1 = 50$ nm and $d_2 = 1$ μ m. For the YIG saturation magnetization we take the literature value $\mu_0 M_{s,2} = 0.18$ T [30]. In Fig. 3 (a) we show the simulations for the YIG/Co(50) sample using $\tau_F = 30$ A s/m², $\tau_D = 15$ A s/m² and $J = -400$ μ J/m². The interfacial exchange constant $J < 0$ models an antiferromagnetic coupling as suggested by the SQUID measurements. The sign of the damping-like torque is required to be positive, as it depends on the real part of the spin mixing conductance of the interface. The simulation reproduces all salient features observed in the experiment, in particular the appearance of the YIG PSSWs and their avoided crossing with the Co FMR line. Note that the simulations do not reproduce the YIG FMR, as we only simulate the Co susceptibility. However, we can obtain a similar color plot for a ferromagnetic coupling and a negative field-like torque (see for example S6, S10 [15]). The combination of exchange torques with the field-like torques at the FM₁|FM₂ interface complicates the analysis of the total coupling because both torques affect the coupling in very similar ways. Hence, the signs of the field-like torque and the exchange torque cannot be determined unambiguously for the YIG/Co(50) sample.

In Fig. 3 (b) we show the simulations for the YIG/Cu(5)/Co(50) sample. Here, τ_F and τ_D are unchanged compared to the values used for the simulation of the YIG/Co(50) sample, but we set $J = 0$, as no static coupling was observed for YIG/Cu(5)/Co(50) in the SQUID measurements. The simulation is in excellent agreement with the corresponding measurement shown in Fig. 1 (b). The elimination of the static exchange coupling results in a strong reduction of the coupling between the YIG and Co magnetization dynamics. However, the Cu layer is transparent to spin currents mediating the field-like and

damping-like torques, as the spin-diffusion length of Cu is much larger than its thickness [31]. We note that a finite field-like torque is necessary to observe the excitation of the PSSWs for vanishing exchange coupling J . Furthermore, the field-like torque is required to be positive to model the intensity asymmetry in the mode branches of the YIG/Cu(5)/Co(50) sample (cf. Fig. S10 [15]).

In Fig. 3 (c) we use $\tau_F = \tau_D = J = 0$, which reproduces the experimental observation for the YIG/AlOx/Co(50) sample. Importantly, no YIG PSSWs are observed in either the experiment or the simulation for this case. In summary, the simulations are in excellent qualitative agreement with the experimental observation of spin dynamics in the coupled YIG/Co heterostructures.

We attribute small quantitative discrepancies between the simulation and the experiment to the fact that we do not take any inhomogeneous linewidth and two-magnon scattering into account, which is, however, present in our system (see S7 [15] for details). This results in an underestimated linewidth of the Co FMR line, in particular for small frequencies. As $|\partial_D S_{21}/\partial H|$ is inversely proportional to the linewidths, this causes small quantitative deviations of the simulations and the experimental data. Furthermore, the exchange modes in Fig. 1 (a) are not found in the simulations. We attribute this to the fact that the simulations only represent the Co susceptibility. However, as shown in Fig. S10 [15], similar exchange modes can also be found in the Co susceptibility from our simulations.

In conclusion, we investigated the dynamic magnetization coupling in YIG/Co heterostructures using broadband ferromagnetic resonance spectroscopy. We find exchange dominated PSSWs in the YIG, excited by spin currents from the Co layer, and static interfacial exchange coupling of YIG and Co magnetizations. An efficient excitation of YIG PSSWs, even with a homogeneous external magnetic driving field, is found in YIG/Co(35),

YIG/Co(50) and YIG/Cu(5)/Co(50) samples, but is suppressed completely in YIG/AlO_x(1.5)/Co(50). We model our observations with a modified Landau-Lifshitz-Gilbert equation, which takes field-like and damping-like torques as well as direct exchange coupling into account.

Our findings pave the way for magnonic devices which operate in the exchange spin-wave regime. Such devices allow for utilization of the isotropic spin-wave dispersion relations in 2D magnonic structures. An excitation of short-wavelength spin waves by an interfacial spin torque does not require any microstructuring of excitation antennas but is in operation in simple magnetic bilayers. Remarkably, this spin torque scheme allows for the coupling of spin dynamics in a ferrimagnetic insulator from that in a ferromagnetic metal. The coupling is qualitatively different to that found for all-metallic heterostructures [13]. Furthermore, the excitation of magnetization dynamics by interfacial torques should allow for efficient manipulation of microscopic magnetic textures, such as magnetic

skyrmions.

Financial support from the DFG via SPP 1538“Spin Caloric Transport” (project GO 944/4 and GR 1132/18) is gratefully acknowledged. S.K. would like to thank Meike Müller for fruitful discussions. V.A. acknowledges support under the Cooperative Research Agreement between the University of Maryland and the National Institute of Standards and Technology, Center for Nanoscale Science and Technology, Award 70NANB14H209, through the University of Maryland.

Note added. - During the review process of this manuscript we became aware of Ref. [32], where avoided crossings are observed between the PSSWs of a 295 nm-thick YIG film and the the FMR line of a CoFeB film. We furthermore became aware of Ref. [33] where avoided crossings are observed between propagating spin waves of a 20 nm-thick YIG film and the FMR line of ferromagnetic nanowires. Both reports support the importance of the exchange interlayer coupling if both magnetic films are in direct contact to each other.

-
- [1] A. Khitun, M. Bao, and K. Wang, *IEEE Transactions on Magnetics* **44**, 2141 (2008).
- [2] A. A. Serga, A. V. Chumak, and B. Hillebrands, *Journal of Physics D: Applied Physics* **43**, 264002 (2010).
- [3] A. V. Chumak, A. A. Serga, and B. Hillebrands, *Nature Communications* **5**, 4700 (2014).
- [4] S. Klingler, P. Pirro, T. Brächer, B. Leven, B. Hillebrands, and A. V. Chumak, *Applied Physics Letters* **105**, 152410 (2014).
- [5] S. Klingler, P. Pirro, T. Brächer, B. Leven, B. Hillebrands, and A. V. Chumak, *Applied Physics Letters* **106**, 212406 (2015).
- [6] K. Ganzhorn, S. Klingler, T. Wimmer, S. Geprägs, R. Gross, H. Huebl, and S. T. B. Goennenwein, *Applied Physics Letters* **109**, 022405 (2016).
- [7] K. Wagner, A. Kákay, K. Schultheiss, A. Henschke, T. Sebastian, and H. Schultheiss, *Nature Nanotechnology* **11**, 432 (2016).
- [8] A. V. Chumak, V. I. Vasyuchka, A. A. Serga, and B. Hillebrands, *Nature Physics* **11**, 453 (2015).
- [9] T. Fischer, M. Kewenig, D. A. Bozhko, A. A. Serga, I. I. Syvorotka, F. Ciubotaru, C. Adelman, B. Hillebrands, and A. V. Chumak, *Applied Physics Letters* **110**, 152401 (2017).
- [10] K. Vogt, F. Fradin, J. Pearson, T. Sebastian, S. Bader, B. Hillebrands, A. Hoffmann, and H. Schultheiss, *Nature Communications* **5**, 1 (2014).
- [11] H. Yu, O. d’Allivy Kelly, V. Cros, R. Bernard, P. Bortolotti, A. Anane, F. Brandl, F. Heimbach, and D. Grundler, *Nature Communications* **7**, 11255 (2016).
- [12] H. Skarsvåg, A. Kapelrud, and A. Brataas, *Physical Review B* **90**, 094418 (2014).
- [13] B. Heinrich, Y. Tserkovnyak, G. Woltersdorf, A. Brataas, R. Urban, and G. E. W. Bauer, *Physical Review Letters* **90**, 187601 (2003).
- [14] S. S. Kalarickal, P. Krivosik, M. Wu, C. E. Patton, M. L. Schneider, P. Kabos, T. J. Silva, and J. P. Nibarger, *Journal of Applied Physics* **99**, 093909 (2006).
- [15] See Supplemental Material [url] for details of sample preparation, experimental setup, data processing, determination of the material parameters, transmission spectra of YIG/Co(35), linewidth analysis, dynamic spin torque theory, and the interfacial spin torque model, which includes Refs. [34–45].
- [16] H. Maier-Flaig, S. T. B. Goennenwein, R. Ohshima, M. Shiraishi, R. Gross, H. Huebl, and M. Weiler, (2017), [arXiv:1705.05694](https://arxiv.org/abs/1705.05694).
- [17] D. C. Crew, K. J. Kennewell, M. J. Lwin, R. C. Woodward, S. Prasad, and R. L. Stamps, *Journal of Applied Physics* **97** (2005), 10.1063/1.1849551.
- [18] M. Belmuguenai, T. Martin, G. Woltersdorf, M. Maier, and G. Bayreuther, *Physical Review B* **76**, 104414 (2007).
- [19] S. Li, C. Wang, X.-M. Chu, G.-X. Miao, Q. Xue, W. Zou, M. Liu, J. Xu, Q. Li, Y. Dai, S. Yan, S. Kang, Y. Long, and Y. Lü, *Scientific Reports* **6**, 33349 (2016).
- [20] D. C. Crew and R. L. Stamps, *Journal of Applied Physics* **93**, 6483 (2003).
- [21] K. L. Livesey, D. C. Crew, and R. L. Stamps, *Physical Review B* **73**, 184432 (2006).
- [22] M. T. Johnson, S. T. Purcell, N. W. E. McGee, R. Coehoorn, J. aan de Stegge, and W. Hoving, *Physical Review Letters* **68**, 2688 (1992).
- [23] M. Vohl, J. Barnaś, and P. Grünberg, *Physical Review B* **39**, 12003 (1989).
- [24] J. Xiao and G. E. W. Bauer, *Physical Review Letters* **108**, 217204 (2012).
- [25] G. Rado and J. Weertman, *Journal of Physics and Chemistry of Solids* **11**, 315 (1959).
- [26] S. Klingler, A. V. Chumak, T. Mewes, B. Khodadadi, C. Mewes, C. Dubs, O. Surzhenko, B. Hillebrands, and A. Conca, *Journal of Physics D: Applied Physics* **48**, 015001 (2015).
- [27] A. G. Gurevich and A. N. Anisimov, *Sov Phys JETP* **41**, 336 (1975).

- [28] C. Dubs, O. Surzhenko, R. Linke, A. Danilewsky, U. Brückner, and J. Dellith, *Journal of Physics D: Applied Physics* **50**, 204005 (2017).
- [29] G. Carlotti, G. Gubbiotti, L. Pareti, G. Socino, and G. Turilli, *Journal of Magnetism and Magnetic Materials* **165**, 424 (1997).
- [30] P. Hansen, P. Röschmann, and W. Tolksdorf, *Journal of Applied Physics* **45**, 2728 (1974).
- [31] S. Yakata, Y. Ando, T. Miyazaki, and S. Mizukami, *Japanese Journal of Applied Physics* **45**, 3892 (2006).
- [32] H. Qin, S. J. Hämmäläinen, and S. van Dijken, (2017), [arXiv:1712.08204](https://arxiv.org/abs/1712.08204).
- [33] J. Chen, C. Liu, T. Liu, Y. Xiao, K. Xia, G. E. W. Bauer, M. Wu, and H. Yu, unpublished.
- [34] S. Pütter, S. Geprägs, R. Schlitz, M. Althammer, A. Erb, R. Gross, and S. T. B. Goennenwein, *Applied Physics Letters* **110**, 012403 (2017).
- [35] M. A. W. Schoen, J. M. Shaw, H. T. Nembach, M. Weiler, and T. J. Silva, *Physical Review B* **92**, 184417 (2015).
- [36] A. J. Berger, E. R. J. Edwards, H. T. Nembach, J. M. Shaw, A. D. Karenowska, M. Weiler, and T. J. Silva, *Physical Review B* **97**, 09440 (2018).
- [37] P. F. Herskind, A. Dantan, J. P. Marler, M. Albert, and M. Drewsen, *Nature Physics* **5**, 494 (2009).
- [38] P. Landeros and D. L. Mills, *Physical Review B* **85**, 054424 (2012).
- [39] M. Körner, K. Lenz, R. A. Gallardo, M. Fritzsche, A. Mücklich, S. Facsko, J. Lindner, P. Landeros, and J. Fassbender, *Physical Review B* **88**, 054405 (2013).
- [40] M. Krawczyk, S. Mamica, M. Mruczkiewicz, J. W. Klos, S. Tacchi, M. Madami, G. Gubbiotti, G. Duerr, and D. Grundler, *Journal of Physics D: Applied Physics* **46**, 495003 (2013).
- [41] R. A. Gallardo, A. Banholzer, K. Wagner, M. Körner, K. Lenz, M. Farle, J. Lindner, J. Fassbender, and P. Landeros, *New Journal of Physics* **16**, 023015 (2014).
- [42] R. Arias and D. L. Mills, *Physical Review B* **60**, 7395 (1999).
- [43] R. McMichael and P. Krivosik, *IEEE Transactions on Magnetics* **40**, 2 (2004).
- [44] R. D. McMichael, *Journal of Applied Physics* **103**, 07B114 (2008).
- [45] H. Maier-Flaig, M. Harder, R. Gross, H. Huebl, and S. T. B. Goennenwein, *Physical Review B* **94**, 054433 (2016).

Supplemental Material: Spin-torque excitation of perpendicular standing spin waves in coupled YIG/Co heterostructures

Stefan Klingler,^{1,2,*} Vivek Amin,^{3,4} Stephan Geprägs,^{1,2} Kathrin Ganzhorn,^{1,2} Hannes Maier-Flaig,^{1,2} Matthias Althammer,^{1,2} Hans Huebl,^{1,2,5} Rudolf Gross,^{1,2,5} Robert D. McMichael,³ Mark D. Stiles,³ Sebastian T.B. Goennenwein,^{6,7} and Mathias Weiler^{1,2,†}

¹Walther-Meißner-Institut, Bayerische Akademie der Wissenschaften, 85748 Garching, Germany

²Physik-Department, Technische Universität München, 85748 Garching, Germany

³Center for Nanoscale Science and Technology, National Institute of Standards and Technology, Gaithersburg, Maryland 20899-6202, USA

⁴Institute for Research in Electronics and Applied Physics, University of Maryland, College Park, MD 20742

⁵Nanosystems Initiative Munich, 80799 Munich, Germany

⁶Institut für Festkörperphysik, Technische Universität Dresden, 01062 Dresden, Germany

⁷Center for Transport and Devices of Emergent Materials, Technische Universität Dresden, 01062 Dresden, Germany

S1. SAMPLE PREPARATION

The commercially available YIG samples are grown by liquid-phase epitaxy on a (111)-oriented gallium gadolinium garnet substrate to a YIG thickness of $d_2 = 1 \mu\text{m}$. Each sample is cut to lateral dimensions of $(6 \times 5) \text{ mm}^2$ and is cleaned with Piranha etch and subsequently annealed in oxygen at $500 \text{ }^\circ\text{C}$ for 40 min [?]. For the first set of samples a thin Co film is deposited onto the YIG film *in-situ* via electron beam evaporation without breaking vacuum. These samples have thicknesses of $d_1 = 35 \text{ nm}$ and $d_1 = 50 \text{ nm}$ (samples YIG/Co(35) and YIG/Co(50), respectively). For a second set of samples a Cu layer with a thickness of $d_s = 5 \text{ nm}$ is evaporated on the YIG before a Co film with a thickness of $d_1 = 50 \text{ nm}$ is grown on top of it (YIG/Cu(5)/Co(50)). Finally, a control sample is prepared, where a $d_s = 1.5 \text{ nm}$ thick aluminum (Al) film is sputtered on the YIG with subsequent oxidation. A Co film with a thickness of $d_1 = 50 \text{ nm}$ is subsequently deposited on top of the insulating AlOx via electron beam evaporation (YIG/AlOx(1.5)/Co(50)). All samples are capped with a 2.5 nm thick layer of AlOx to prevent oxidation of the Co layer.

S2. EXPERIMENTAL SETUP

The dynamic magnetization properties are measured using a vector network analyzer (VNA)-based broadband ferromagnetic resonance setup at room temperature. Fig. S2 shows a sketch of the measurement setup. The YIG/Co samples are placed on a coplanar waveguide (CPW) with the Co side down. The center conductor of the CPW has a width of $w = 300 \mu\text{m}$. The CPW is positioned between the pole shoes of an electromagnet, where magnetic fields

of up to 3 T can be applied. The CPW is connected to ports 1 and 2 (P1 and P2, respectively) of the VNA and the complex-valued transmission of a microwave current j_{rf} is measured in a frequency range between $f = 1 \text{ GHz}$ and $f = 26.5 \text{ GHz}$ as a function of the applied magnetic field for a fixed microwave power of 0 dBm. When the applied frequency f matches the resonance condition for a given field \mathbf{H} , microwave power is absorbed, which results in a precession of the samples magnetization. As the transmission signal of the CPW is strongly frequency dependent, we do not show the raw frequency spectra in the main text, but the field-derivative of S_{21} as shown in Ref. [?] and S3.

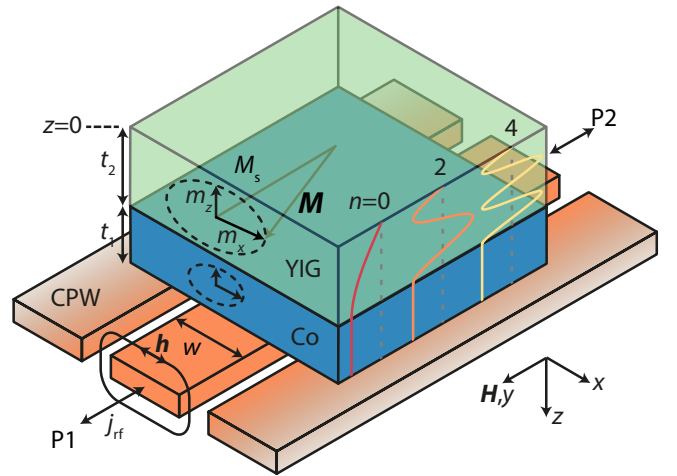


FIG. S2. Sketch of the measurement setup. The YIG/Co samples are positioned with the Co-side down onto the center conductor of the CPW.

* stefan.klingler@wmi.badw.de

† mathias.weiler@wmi.badw.de

S3. DERIVATIVE DIVIDE - EXPERIMENT AND SIMULATIONS

The measured transmission of the vector network analyzer is given by:

$$S_{21}(H) = \Delta S_{21}(H)S_{21}^0 + S_{21}^0. \quad (\text{S3.1})$$

Here, S_{21}^0 is the field-independent background transmission. Note that a perfect background transmission is achieved for $S_{21}^0 = 1$. The measurement signal is given by [?]:

$$\Delta S_{21}(H) = -i\omega \frac{L_0(H)}{2Z_0}, \quad (\text{S3.2})$$

where L_0 is the inductance of the sample and $Z_0 = 50 \Omega$ is the microwave circuit impedance. The sample inductance is given by [?]:

$$L_0(H) = \frac{\mu_0 l d_{\text{tot}}}{4w} \chi(H), \quad (\text{S3.3})$$

where $l = 5 \text{ mm}$ is the length of the sample, $d_{\text{tot}} \approx 1 \mu\text{m}$ is the total thickness of the sample, $w = 300 \mu\text{m}$ is the width of the center conductor, and $\chi(H)$ is the dynamic magnetic susceptibility.

The background-corrected field derivative of our measurement signal is now given by [?]:

$$\partial_{\text{D}} S_{21} / \partial H = \frac{1}{S_{21}(H)} \frac{S_{21}(H + \delta H) - S_{21}(H - \delta H)}{\delta H}, \quad (\text{S3.4})$$

where δH is a constant field step in our measurement of about 0.5 mT. Note that the differential quotient is rescaled by the central value $S_{21}(H)$ which eliminates background drift.

We simulate $\chi = \chi_{1,xx}$, from which we calculate ΔS_{21} with Eq. (S3.2), where $\chi_{1,xx}$ creates the x -component of the dynamic magnetization in the limit of $w > d_{\text{tot}}$. To compare the simulation results to experimental data, we use Eq. (S3.1) with $S_{21}^0 = 1$ and then calculate $\partial_{\text{D}} S_{21} / \partial H$ from Eq. (S3.3) which yields:

$$\begin{aligned} \partial_{\text{D}} S_{21} / \partial H &= \frac{\Delta S_{21}(H + \delta H) - \Delta S_{21}(H - \delta H)}{(\Delta S_{21}(H) + 1)\delta H} \\ &= \frac{d_{\text{tot}} l \mu_0 \omega (\chi_{1,xx}(\delta H + H) - \chi_{1,xx}(H - \delta H))}{\delta H (d_{\text{tot}} l \mu_0 \omega \chi_{1,xx}(H) + 8i w Z_0)}. \end{aligned} \quad (\text{S3.5})$$

The susceptibility element $\chi_{1,xx}$ is derived in S9.

S4. DETERMINATION OF MATERIAL PARAMETERS

Fig. S4(a) shows the extracted resonance fields as a function of the frequency for the YIG/Co(35) sample using a fit of up to five superimposed Lorentzian resonances.

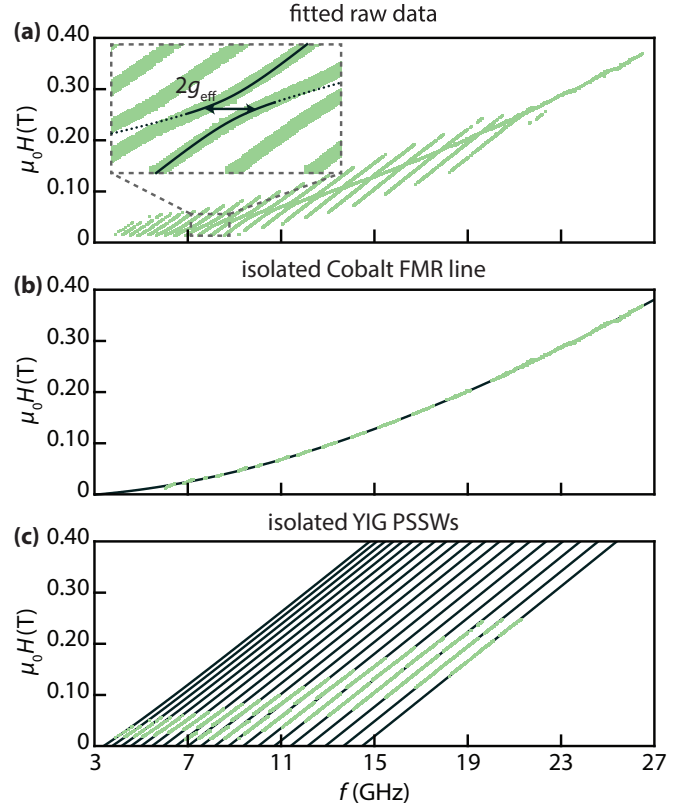


FIG. S4. (a) Fitted raw data resonance fields and frequencies of the YIG/Co(35) sample. (b) Isolated Co FMR line. (c) Isolated YIG PSSWs.

The inset shows a magnification of the field and frequency range marked with the dashed box, and we observe multiple avoided crossings. The frequency splitting g_{eff} is determined using a fit of a coupled harmonic oscillator model to the avoided crossings, as shown in [?].

To obtain the material parameters of the Co layer, we fit the pure Co FMR line which we get by deleting all data points of avoided crossings and YIG PSSWs from the data set, as shown in Fig. S4(b). For the fit we use the in-plane Kittel equation,

$$f_i = \frac{\mu_0 \gamma_i}{2\pi} \sqrt{(H + H_{\text{ex},i})(H + H_{\text{ex},i} + M_{s,i})} \quad (\text{S4.1})$$

which yields $\gamma_1/2\pi = 28.7(1) \text{ GHz/T}$ and $\mu_0 M_{s,1} = 1.91(2) \text{ T}$, where the number in brackets denotes the error of the last digit. The fit is shown as a black line.

To obtain the material parameters of the YIG film, we fit the pure YIG PSSWs, as shown in Fig. S4(c). We keep $\mu_0 M_{s,2} = 0.18 \text{ T}$ constant, as we otherwise get a mutual dependence of $M_{s,2}$ and $H_{\text{ex},2}$ during the fit [?]. A global fit, where γ_1 in Eq. (S4.1) is a shared fit parameter and $H_{\text{ex},i}$ is fitted for each PSSW individually, yields $\gamma_2/2\pi = 27.07(1) \text{ GHz/T}$. The fits are shown as black lines.

The values of the YIG and the Co film agree very well

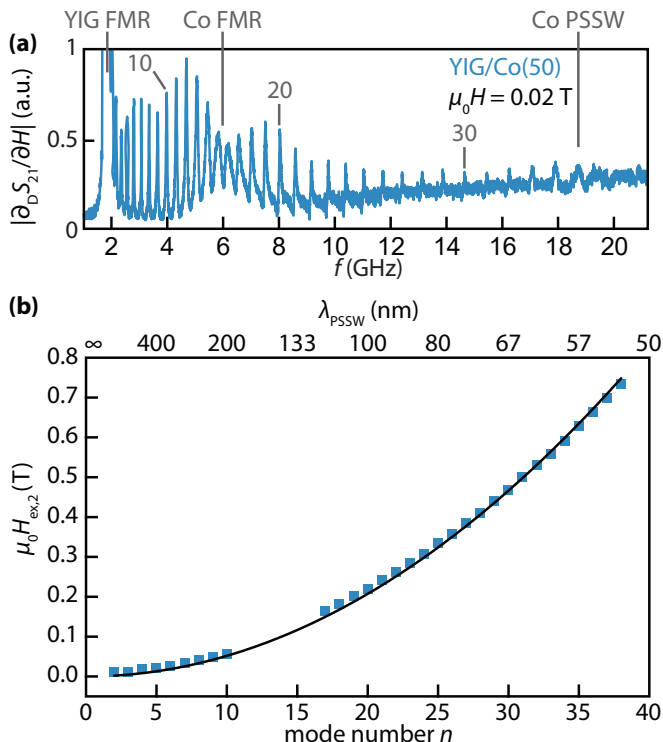


FIG. S5. (a) Example frequency spectrum of the YIG/Co(50) sample at $\mu_0 H = 0.02$ T. (b) The extracted exchange fields of the YIG/Co(50) sample are plotted as a function of the PSSW mode number n .

with the literature values [? ? ? ?] and they are thus taken to be constant throughout for the data analysis.

S5. DETERMINATION OF THE EXCHANGE STIFFNESS

In Fig. S5 (a), an example frequency spectrum is shown for the YIG/Co(50) sample for a fixed field of $\mu_0 H = 0.02$ T. Plotted is $|\partial_D S_{21} / \partial H|$ versus applied microwave frequency, and the plot corresponds to a cut along the x -axis in Fig. 1 (a). The peak in $|\partial_D S_{21} / \partial H|$ at 2 GHz is attributed to the YIG FMR frequency. At about 6 GHz we find a broad excitation of the Co FMR. Furthermore, we resolve about 40 YIG PSSW resonances. Some of the YIG PSSWs are labeled to guide the reader. In comparison to Ref. [?] we find a drastically increased sensitivity for the YIG PSSWs. Furthermore, all PSSWs are equally visible, not only the modes with an odd mode number. This is expected for driving fields which are strongly inhomogeneous, but cannot be explained with the width of the used center conductor, which is much larger than the YIG film thickness.

From the extracted resonance fields of each YIG mode, we are able to determine the exchange fields, see S4. For this we assume a fixed saturation magnetization of $\mu_0 M_{s,2} = 0.18$ T [?]. We then use the method proposed

in Ref. [?] to determine the exchange stiffness D_s . In Fig. S5 (b), the extracted exchange fields are shown as a function of the mode number n . We see a quadratic curvature (black) of the exchange field, which is fitted using:

$$\mu_0 H_{ex,2} = D_{s,2} \left(\frac{n\pi}{d_2} \right)^2. \quad (S5.1)$$

From the fit a value of $D_{s,2} = 5.25(2) \times 10^{-17}$ T m² is obtained, which is in very good agreement with previously reported values [? ?]. Using the relation $A_i = D_{s,i} M_{s,i} / 2$ we yield $A_2 = A = 3.76$ pJ/m. Furthermore, the quadratic increase of the exchange fields with the mode number n and the extracted value of $D_{s,i}$ confirm our assumption that we indeed observe standing spin-wave modes in the YIG film. Note that we only expect minor interfacial corrections to for $H_{ex,2}(k)$ for mixed boundary conditions.¹

S6. TRANSMISSION SPECTRA YIG/Co(35)

Fig. S6 (a) shows the background-corrected field derivative of the transmission spectra for the YIG/Co(35) heterostructure. Again we observe the high and the low frequency mode which correspond to the Co and YIG FMR lines, respectively, together with the exchange mode. The YIG PSSWs form avoided crossings with the Co FMR line as shown in magnification (inset). The frequency splitting has about the same size as found from the YIG/Co(50) heterostructure and be simulated with similar parameters. Here, we show that these parameters are not unique. Fig. S6 (b) shows the simulation for the YIG/Co(35) heterostructure using a negative field-like torque and a ferromagnetic coupling, in contrast to the simulations in the main text. This parameter set also models the avoided crossings. However, the intensity asymmetry of the avoided crossings is only reproduced with the ferromagnetic coupling if the field-like torque is negative, as shown in Fig. S6 (b). For more details, see S10.

S7. CO LINEWIDTH EVOLUTION OF THE YIG/AlOx(1.5)/Co(50) SAMPLE

In this section we analyze the linewidth evolution of the YIG/AlOx/Co(50) sample and compare it to the YIG/Co(50) sample to show that the magnetizations are uncoupled. Even a weak coupling of the YIG and the Co

¹ If we assume total pinning of the YIG magnetization at both interfaces, we obtain a small deviation of 4 % to the extracted value of $D_{s,2}$.

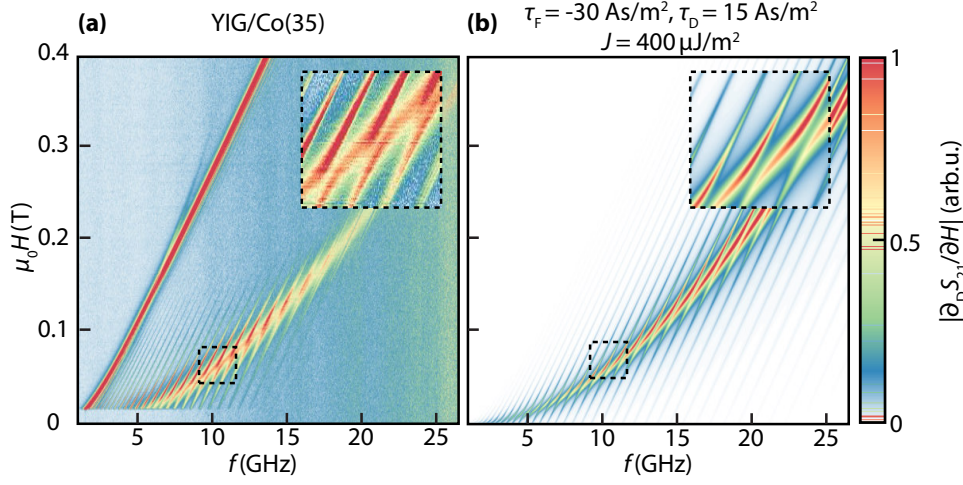


FIG. S6. (a) Transmission spectra of the YIG/Co(35). (b) Simulation of the of the YIG/Co(35) sample using the inverted field-like and exchange torques as in the main text for the YIG/Co(50) sample.

magnetizations should be visible in the linewidth evaluations of the subsystems [? ?], as the coupling opens additional relaxation channels, which is reflected in the lifetimes of the spin-wave resonances. In Fig. S7 the linewidth evolution of the YIG/Co(50) sample is shown as a function of the excitation frequency (blue symbols). We find for $f < 14$ GHz a strong modulation of the linewidth. This modulation goes along with the observation of avoided crossings in Fig. 1 (a). However, in Fig. S7 also the Co linewidth from the YIG/AlOx(1.5)/Co(50) sample (orange symbols) is shown as a function of the excitation frequency. For small frequencies we see a fast increase of

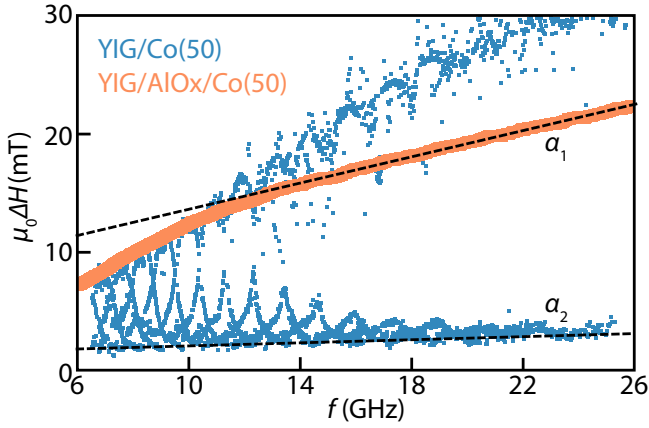


FIG. S7. The linewidth evolution of the YIG/Co(50) and YIG/AlOx(1.5)/Co(50) samples is shown as a function of the excitation frequency. The linewidth of the YIG/AlOx(1.5)/Co(50) sample increases monotonically (orange symbols), without any modulation. The blue symbols show the linewidths of the YIG/Co(50) sample which shows characteristic modulation for every coupled PSSW.

the linewidth which flattens out above $f = 10$ GHz. The shape of this linewidth evolution can be understood with Gilbert damping and two-magnon scattering processes, which are expected for an in-plane measurement geometry [? ? ? ? ? ?]. There are no additional features that indicate any coupling of the YIG and the Co in the YIG/AlOx(1.5)/Co(50) heterostructure. Hence, we can rule out dynamic stray fields as the origin of the coupling. From the YIG/AlOx(1.5)/Co(50) sample we extract a Gilbert damping parameter α_1 of the Co layer using the Gilbert damping equation [?]:

$$\mu_0 \Delta H_i = \mu_0 \Delta H_{0,i} + \frac{4\pi\alpha_i}{\gamma_i} f, \quad (\text{S7.1})$$

where ΔH_1 is the Co linewidth and $\Delta H_{0,1}$ the inhomogeneous line broadening of the Co film. The fit is shown as the black dashed line in Fig. S7 and we obtain an intrinsic Gilbert damping of $\alpha_1 = 0.0077 \pm 0.0001$ and $\mu_0 \Delta H_{0,1} = (8 \pm 1)$ mT. Hence, approximately half of the linewidth of the Co resonance is due to the frequency independent inhomogeneous line broadening. The YIG damping can be estimated in a similar way from the coupled YIG/Co(50) sample to be $\alpha_2 = (7.2 \pm 0.3) \times 10^{-4}$, which is in good agreement with previous reports [?] .

S8. DYNAMIC SPIN TORQUE IN A FM₁|NM|FM₂ HETEROSTRUCTURE

We write the following equations in terms of the magnetization density and magnetization current. We assume a large applied field in the y -direction which aligns the magnetization. The film lies in the $x - y$ -plane, whereas the film normal points along the z -direction (S2). We also assume that the transverse magnetizations are small and decouple from the charge and longitudinal magneti-

zation. It is convenient to write the equations of motion in terms of complex numbers made up of the transverse components. Thus we express the vector $\mathbf{f} = (f_x, 1, f_z)$ as follow:

$$\mathbf{f}_\perp = f_z + if_x \leftrightarrow \begin{pmatrix} \text{Re} [f_\perp] \\ \text{Im} [f_\perp] \end{pmatrix} = \begin{pmatrix} f_z \\ f_x \end{pmatrix}. \quad (\text{S8.1})$$

In this notation, the cross product operation $(0, 1, 0) \times (f_x, 1, f_z) = (f_z, 0, -f_x)$ can be represented as multiplication with the imaginary unit i

$$(\hat{\mathbf{y}} \times \mathbf{f})_\perp \rightarrow -f_x + if_z = i(f_z + if_x) = if_\perp. \quad (\text{S8.2})$$

In the following we drop the subscript \perp from the complex representation of vectors (without serifs and upright) for simplicity.

We consider a ferromagnet|normal metal|ferromagnet (FM₁|NM|FM₂) heterostructure, where the spacer layer d_s is thick compared to its mean free path but thin compared to the spin diffusion length. The first assumption allows us to use the drift-diffusion approach to treat the transport. The second assumption allows us to neglect spin-flip scattering in the spacer layer, in which case the spin accumulation varies linearly across the spacer layer. In this case the transverse spin current density $\mathbf{j} = 2eQ/\hbar$ (in units of V, the traditional spin current density is given by Q) in the spacer layer can be written as follows:

$$\begin{aligned} \mathbf{j}(z) &= -D\nabla\mu(z) \\ &= -D\nabla(\mu_0 + \mu'z) \\ &= -D\mu'. \end{aligned} \quad (\text{S8.3})$$

Here, $\mu(z) = (\mu_\uparrow - \mu_\downarrow)/e$ is the spin accumulation in the spacer (units of V), also written as a complex number; and $D = \sigma_{\text{NM}}$ (units of $1/\Omega\text{m}$), where σ_{NM} is the bulk conductivity of the normal metal. Note that we work with spin accumulation rather than spin density; this gives the constant D units of $1/\Omega\text{m}$ rather than m^2/s . In the second line we have used a linear expansion of the spin accumulation, where $\mu' = \partial\mu/\partial z$. We find that the spatially-constant spin current density is proportional to the gradient of the spin accumulation.

We assume the spacer layer has length d_s , running from $z = -d_s/2$ to $z = d_s/2$ (Without loss of generality, we have shifted here the origin of the coordinate system to the center of the spacer layer, in contrast to the other sections). For the boundary conditions at the first interface ($z = -d_s/2$), we have

$$\begin{aligned} -D\mu' &= \mathbf{j}(-d_s/2) \\ &= -G_1\mu + \frac{\hbar}{e}G_1i\dot{\mathbf{m}}_1 \\ &= -G_1(\mu_0 - \mu'd_s/2) + \frac{\hbar}{e}G_1i\dot{\mathbf{m}}_1. \end{aligned} \quad (\text{S8.4})$$

Here, G_1 is the complex spin mixing conductance of the first interface (units of $1/\Omega\text{m}^2$). The top line gives the spin current in the spacer layer and the second line is

the boundary condition from magnetoelectronic circuit theory with the second term the pumped spin current. In the second line, we have used $\mathbf{M}_1 \times \mathbf{M}_1 \approx \hat{\mathbf{y}} \times \dot{\mathbf{M}}_1 \rightarrow i\dot{\mathbf{m}}_1$. The boundary condition at the other interface ($z = d_s/2$) is the same except that the signs change because the direction of the interface normal changes:

$$\begin{aligned} \mathbf{j}(d_s/2) &= -D\mu' \\ &= G_2(\mu_0 + \mu'd_s/2) - \frac{\hbar}{e}G_2i\dot{\mathbf{m}}_2. \end{aligned} \quad (\text{S8.5})$$

The boundary conditions then give us four equations in four unknowns ($\mu_{0z}, \mu_{0x}, \mu'_z, \mu'_x$), or two complex equations Eq. (S8.4) and Eq. (S8.5) in two complex unknowns (μ_0, μ'). We find

$$\begin{aligned} \mu_0 &= \frac{i\hbar 2D(G_1\dot{\mathbf{m}}_1 + G_2\dot{\mathbf{m}}_2) + d_sG_1G_2(\dot{\mathbf{m}}_1 + \dot{\mathbf{m}}_2)}{e 2(D(G_1 + G_2) + d_sG_1G_2)}, \\ \mu' &= -\frac{iG_1G_2\hbar(\dot{\mathbf{m}}_1 - \dot{\mathbf{m}}_2)}{e(D(G_1 + G_2) + d_sG_1G_2)}, \end{aligned} \quad (\text{S8.6})$$

from which we can derive the spin current

$$\mathbf{j}(-d_s/2) = -i\frac{\hbar}{e}G(\dot{\mathbf{m}}_1 - \dot{\mathbf{m}}_2). \quad (\text{S8.7})$$

Here we have defined an effective mixing conductance that describes the coupled system:

$$G = \frac{G_1G_2}{G_1 + G_2 + G_1G_2d_s/D} \approx \frac{G_1G_2}{G_1 + G_2}, \quad (\text{S8.8})$$

where we have used the small d_s limit in the second step in the denominator, as the conductance of a thin Cu layer is much greater than either mixing conductance (the Cu interlayer is much thinner than the spin-diffusion length of Cu). Note that in this limit the amplitudes of the spin currents persist, when we remove the Cu layer. However, in this case the exchange coupling starts to play a major role.

In the absence of spin-orbit coupling, the spin torque exerted on some region equals the difference between the spin currents at the boundaries of that region. The transverse spin current just inside the ferromagnets vanish due to dephasing, i.e., $\mathbf{j}(-d_s/2 - \epsilon) = 0$ and $\mathbf{j}(d_s/2 + \epsilon) = 0$. So, the spin torque, τ_1 , also a complex number representing the two transverse components, at the first interface is given by

$$\begin{aligned} \tau_1 &= \Delta\mathbf{j} \\ &= \mathbf{j}(-d_s/2 + \epsilon) - \mathbf{j}(-d_s/2 - \epsilon) \\ &= \mathbf{j}(-d_s/2 + \epsilon), \end{aligned} \quad (\text{S8.9})$$

where the x and z components are extracted according to the prescription given above:

$$\tau_{1,z} = \text{Re}[\mathbf{j}], \quad (\text{S8.10})$$

$$\tau_{1,x} = \text{Im}[\mathbf{j}]. \quad (\text{S8.11})$$

Since the interface normal flips between the two interfaces, the torques on the two magnetizations are equal and

opposite (i.e., $\tau_1 = -\tau_2$). Note that here the torques have the same units as the normalized spin current density.

We now want to show how the spin torques are included in the Landau-Lifshitz-Gilbert equation. Assuming a time dependence of the magnetization

$$\mathbf{m}_i = (m_{i,z}, m_{i,x}) \exp(-i\omega t), \quad (\text{S8.12})$$

the spin torque on the first ferromagnet is given by

$$\begin{aligned} \tau_1 &= -i\frac{\hbar}{e}\mathbf{G}(-i\omega)(\mathbf{m}_1 - \mathbf{m}_2) \\ &= -\omega\frac{\hbar}{e}\mathbf{G}(\mathbf{m}_1 - \mathbf{m}_2), \end{aligned} \quad (\text{S8.13})$$

and similarly the spin torque on the second ferromagnet

is given by

$$\tau_2 = \omega\frac{\hbar}{e}\mathbf{G}(\mathbf{m}_1 - \mathbf{m}_2) = -\tau_1. \quad (\text{S8.14})$$

Hence, the torques depend on the real and imaginary parts of the effective mixing conductance \mathbf{G} . Unfortunately, extracting the mixing conductances for each interface is impossible unless one mixing conductance is already known.

In the following we show how the torques can be introduced to the LLG. After a complex multiplication we obtain from Eq. (S8.13) and Eq. (S8.14):

$$\begin{aligned} \tau_{1,z} = \text{Re}[\tau_1] &= -\omega\frac{\hbar}{e}\left(\text{Re}[\mathbf{G}]\text{Re}[\mathbf{m}_1 - \mathbf{m}_2] - \text{Im}[\mathbf{G}]\text{Im}[\mathbf{m}_1 - \mathbf{m}_2]\right) \\ &= -\omega\left(\tau_{\text{D}}(m_{1,z} - m_{2,z}) - \tau_{\text{F}}(m_{1,x} - m_{2,x})\right) \end{aligned} \quad (\text{S8.15})$$

$$\begin{aligned} \tau_{1,x} = \text{Im}[\tau_1] &= -\omega\frac{\hbar}{e}\left(\text{Im}[\mathbf{G}]\text{Re}[\mathbf{m}_1 - \mathbf{m}_2] + \text{Re}[\mathbf{G}]\text{Im}[\mathbf{m}_1 - \mathbf{m}_2]\right) \\ &= -\omega\left(\tau_{\text{F}}(m_{1,z} - m_{2,z}) + \tau_{\text{D}}(m_{1,x} - m_{2,x})\right), \end{aligned} \quad (\text{S8.16})$$

and analogously

$$\tau_{2,z} = \text{Re}[\tau_2] = \omega\left(\tau_{\text{D}}(m_{1,z} - m_{2,z}) - \tau_{\text{F}}(m_{1,x} - m_{2,x})\right) \quad (\text{S8.17})$$

$$\tau_{2,x} = \text{Im}[\tau_2] = \omega\left(\tau_{\text{F}}(m_{1,z} - m_{2,z}) + \tau_{\text{D}}(m_{1,x} - m_{2,x})\right), \quad (\text{S8.18})$$

where we have defined the torque strengths (units of A s/m²) as

$$\tau_{\text{D}} = \frac{\hbar}{e}\text{Re}[\mathbf{G}], \quad (\text{S8.19})$$

$$\tau_{\text{F}} = \frac{\hbar}{e}\text{Im}[\mathbf{G}]. \quad (\text{S8.20})$$

Note that multiplying a torque strength ($\tau_{\text{D}/\text{F}}$) by the time derivative of a magnetization unit vector gives a torque in units of A/m². The torque on the second interface (τ_2) is obtained in a similar manner. The expressions for both torques can be written in matrix notation as follows:

$$\begin{pmatrix} \tau_{1,z} \\ \tau_{1,x} \\ \tau_{2,z} \\ \tau_{2,x} \end{pmatrix} = -\omega \begin{pmatrix} \tau_{\text{D}} & -\tau_{\text{F}} & -\tau_{\text{D}} & \tau_{\text{F}} \\ \tau_{\text{F}} & \tau_{\text{D}} & -\tau_{\text{F}} & -\tau_{\text{D}} \\ -\tau_{\text{D}} & \tau_{\text{F}} & \tau_{\text{D}} & -\tau_{\text{F}} \\ -\tau_{\text{F}} & -\tau_{\text{D}} & \tau_{\text{F}} & \tau_{\text{D}} \end{pmatrix} \begin{pmatrix} m_{1,z} \\ m_{1,x} \\ m_{2,z} \\ m_{2,x} \end{pmatrix}. \quad (\text{S8.21})$$

Here the torques still have units of charge current density. To convert the torque strengths into a form consistent

with the LLG equations, they must be multiplied by

$$-\frac{\hbar\gamma_i}{ed_iM_{s,i}}, \quad (\text{S8.22})$$

where $i \in [1, 2]$ denotes the material, γ_i is the gyromagnetic ratio, $M_{s,i}$ is the saturation magnetization, and d_i is the magnetic film thickness.

S9. THE INTERFACIAL SPIN-TORQUE MODEL

Here, we derive a model for the dynamic mode coupling at the YIG/Co interface. For this we use a macrospin approximation for the Co magnetization (\mathbf{M}_1), as we only consider the first cobalt mode. However, we assume that the unit vector of YIG magnetization direction ($\mathbf{M}_2(z)$) varies spatially. In section S8, a real-valued two-vector was represented as a single complex number. Here, we adopt a notation of using lower case bold letters to indicate the transverse components. In addition, to capture the phases of the precessing moments, we allow these vectors

to be complex with the understanding that the real part should be taken of a results to get physical quantities.

As in the main text, upper case bold characters indicate three-dimensional vectors.

In the limit of small transverse magnetization, the energy of the coupled heterostructure is given by:

$$E = \int_0^{d_2} dz \left[A (\partial_z \mathbf{m}_2)^2 + \frac{\mu_0 H M_{s,2}}{2} \mathbf{m}_2 \cdot \mathbf{m}_2 + \frac{\mu_0 M_{s,2}^2}{2} m_{2,z}^2 \right] + \frac{\mu_0 H M_{s,1} d_1}{2} \mathbf{m}_1 \cdot \mathbf{m}_1 + \frac{\mu_0 M_{s,1}^2 d_1}{2} m_{1,z}^2 + J (\mathbf{m}_1 - \mathbf{m}_2(d_2))^2. \quad (\text{S9.1})$$

Here, the integrand describes the energy contribution of the YIG film. All variable definitions are given in the main text.

We obtain the effective field of the Co by using the magnetic energy which is normalized on the Co thickness and saturation magnetization: $H_{\text{eff},1} = -\nabla E / (M_{s,1} d_1)$. We can hence write down the linearized Landau-Lifshitz-Gilbert equation for the Co film:

$$\dot{\mathbf{m}}_1 = -\gamma_1 \hat{\mathbf{y}} \times \left[-\mu_0 H \mathbf{m}_1 - \frac{\alpha_1}{\gamma_1} \dot{\mathbf{m}}_1 - \mu_0 M_{s,1} M_{1,z} \hat{\mathbf{z}} - \frac{J}{d_1 M_{s,1}} (\mathbf{m}_1 - \mathbf{m}_2(d_2)) + \mu_0 \mathbf{h} \right] - \frac{\hbar \gamma_1}{e d_1 M_{s,1}} [(\tau_F - \tau_D \hat{\mathbf{y}} \times) (\dot{\mathbf{m}}_1 - \dot{\mathbf{m}}_2(d_2))]. \quad (\text{S9.2})$$

Here we have used that the static magnetization lies along in the film plane, parallel to the external magnetic field along the y -direction. Analogously, we derive the equation of motion for the YIG away from the interface:

$$\dot{\mathbf{m}}_2 = -\gamma_2 \hat{\mathbf{y}} \times \left[-\mu_0 H \mathbf{m}_2 - \frac{\alpha_2}{\gamma_2} \dot{\mathbf{m}}_2 - \mu_0 M_{s,2} m_{2,z} \hat{\mathbf{z}} + \frac{2A}{M_{s,2}} \partial_z^2 \mathbf{m}_2 + \mu_0 \mathbf{h} \right], \quad (\text{S9.3})$$

where the definitions of the variables is analogous to the Co variables, except of the index 2 instead of 1. The coupling terms will be treated as a boundary condition.

A. Determination of the Eigenvectors

We know that the magnetization in the YIG is a superposition of the eigenmodes in the undisturbed film. In order to determine those, we start by rewriting Eq. (S9.3) in a notation of the transverse magnetization. By using the ansatz for the transverse magnetization components

$$\mathbf{m}_2 = \exp(ikz) \exp(-i\omega t) \begin{pmatrix} m_{2,z} \\ m_{2,x} \end{pmatrix}, \quad (\text{S9.4})$$

we obtain a system of equations including the YIG susceptibility $\tilde{\chi}_2^{-1}$, which describes the response of the transverse YIG magnetization perpendicular to external magnetic fields:

$$0 = \underbrace{\begin{pmatrix} -i\omega & \gamma_2 \left(\frac{2Ak^2}{M_{s,2}} + \mu_0 H \right) - i\alpha_2 \omega \\ \gamma_2 \left(-\frac{2Ak^2}{M_{s,2}} - \mu_0 H - \mu_0 M_{s,2} \right) + i\alpha_2 \omega & -i\omega \end{pmatrix}}_{\tilde{\chi}_2^{-1}} \begin{pmatrix} m_{2,z} \\ m_{2,x} \end{pmatrix}. \quad (\text{S9.5})$$

The system of equations is solved for $\det \tilde{\chi}_2^{-1} = 0$ by the wavevectors:

$$k = \frac{1}{2} \sqrt{\frac{M_{s,2} \left(2i\alpha_2 \omega - \gamma_2 \mu_0 (2H + M_{s,2}) + \sqrt{\gamma_2^2 \mu_0^2 M_{s,2}^2 + 4\omega^2} \right)}{A\gamma_2}}, \quad (\text{S9.6})$$

$$\kappa = \frac{1}{2} \sqrt{-\frac{M_{s,2} \left(-2i\alpha_2 \omega + \gamma_2 \mu_0 (2H + M_{s,2}) + \sqrt{\gamma_2^2 \mu_0^2 M_{s,2}^2 + 4\omega^2} \right)}{A\gamma_2}}. \quad (\text{S9.7})$$

The wavevector k describes an harmonic oscillation of the magnetization along the z -direction. The wavevector κ on the other side describes an evanescent behavior of the YIG magnetization, with a decay length in the order of 10 nm. We now use the obtained wavevectors in Eq. (S9.5) in order to derive the eigenvectors of the YIG magnetization. For the wavevectors k and κ we obtain

$$k : 0 = \begin{pmatrix} -i\omega & \frac{1}{2} \left(-M_{s,2}\gamma_2\mu_0 + \sqrt{M_{s,2}^2\gamma_2^2\mu_0^2 + 4\omega^2} \right) \\ \frac{1}{2} \left(-M_{s,2}\gamma_2\mu_0 - \sqrt{M_{s,2}^2\gamma_2^2\mu_0^2 + 4\omega^2} \right) & -i\omega \end{pmatrix} \begin{pmatrix} m_{2,z} \\ m_{2,x} \end{pmatrix}, \quad (\text{S9.8})$$

$$\kappa : 0 = \begin{pmatrix} -i\omega & \frac{1}{2} \left(-M_{s,2}\gamma_2\mu_0 - \sqrt{M_{s,2}^2\gamma_2^2\mu_0^2 + 4\omega^2} \right) \\ \frac{1}{2} \left(-M_{s,2}\gamma_2\mu_0 + \sqrt{M_{s,2}^2\gamma_2^2\mu_0^2 + 4\omega^2} \right) & -i\omega \end{pmatrix} \begin{pmatrix} m_{2,z} \\ m_{2,x} \end{pmatrix}. \quad (\text{S9.9})$$

We now take the zero eigenvalue of both systems, as this refers to our resonance condition $\det \tilde{\chi}_2^{-1} = 0$. We find

$$k : \mathbf{m}_{2+} = \begin{pmatrix} \frac{i(-\sqrt{\gamma_2^2\mu_0^2 M_{s,2}^2 + 4\omega^2} + \gamma_2\mu_0 M_{s,2})}{2\omega} \\ 1 \end{pmatrix}, \quad (\text{S9.10})$$

$$\kappa : \mathbf{m}_{2-} = \begin{pmatrix} \frac{i(\sqrt{\gamma_2^2\mu_0^2 M_{s,2}^2 + 4\omega^2} + \gamma_2\mu_0 M_{s,2})}{2\omega} \\ 1 \end{pmatrix}. \quad (\text{S9.11})$$

B. Setup of the Boundary Conditions

We model the YIG/Co interface as an infinitesimally thin surface layer. While the magnetization is not pinned at the interface, the infinitesimally thin layer has no volume and hence no angular momentum. As a consequence, the total torque acting at the interface has to vanish [? ? ?]:

$$0 = 2A\hat{\mathbf{y}} \times \partial_z \mathbf{m}_2(z)|_{z=d_2} - J\hat{\mathbf{y}} \times (\mathbf{m}_1 - \mathbf{m}_2(d_2)) + (\hbar/e)(\tau_F - \tau_D)\hat{\mathbf{y}} \times (\dot{\mathbf{m}}_1 - \dot{\mathbf{m}}_2(d_2)). \quad (\text{S9.12})$$

On the YIG/substrate interface we also set the torques to be zero:

$$0 = 2A\hat{\mathbf{y}} \times \partial_z \mathbf{m}_2(z)|_{z=0} \quad (\text{S9.13})$$

C. Solution of the Problem

The ansatz of the dynamic YIG magnetization \mathbf{m}_2 and the dynamic Co magnetization \mathbf{m}_1 are

$$\mathbf{m}_2 = +c_- \mathbf{m}_{2-} \exp(-i\omega t) \cos(\kappa z) + c_+ \mathbf{m}_{2+} \exp(-i\omega t) \cos(kz), \quad (\text{S9.14})$$

and

$$\mathbf{m}_1 = \begin{pmatrix} m_{z,1} \\ m_{x,1} \end{pmatrix} \exp(-i\omega t). \quad (\text{S9.15})$$

In a first step we rewrite the boundary condition Eq. (S9.12):

$$0 = +2A(-c_- \kappa \mathbf{m}_{2-} \sin(\kappa z) - c_+ k \mathbf{m}_{2+} \sin(kz)) - (\hbar/e)\tau_F \hat{\mathbf{y}} \times (ic_- \mathbf{m}_{2-\omega} \cos(\kappa z) + ic_+ \mathbf{m}_{2+\omega} \cos(kz) - i\mathbf{m}_{1,0\omega}) + (\hbar/e)\tau_D (ic_- \mathbf{m}_{2-\omega} \cos(\kappa z) + ic_+ \mathbf{m}_{2+\omega} \cos(kz) - i\mathbf{m}_{1,0\omega}) - J(-c_- \mathbf{m}_{2-} \cos(\kappa z) - c_+ \mathbf{m}_{2+} \cos(kz) + \mathbf{m}_{1,0}) \quad (\text{S9.16})$$

where we have used $\hat{\mathbf{y}} \times (\hat{\mathbf{y}} \times \mathbf{m}_i) = -\mathbf{m}_i$ in the first step. In the second step we have used Eq. (S9.14), and the fact that the dynamic YIG magnetization must obey the boundary conditions for all times t . To solve for the coefficients c_{\pm} , we multiply the above equation with the complex conjugates of the YIG magnetization eigenvectors $\mathbf{m}_{2\pm}^*$, which obey the special orthogonality relations $\mathbf{m}_{2\mp} \mathbf{m}_{2\pm}^* = 0$. From the multiplication of \mathbf{m}_{2+}^* we obtain:

$$0 = \mathbf{m}_{2+}^* \left[-2Ac_+ k \mathbf{m}_{2+} \sin(kz) - (\hbar/e)\tau_F \hat{\mathbf{y}} \times (ic_- \mathbf{m}_{2-\omega} \cos(\kappa z) + ic_+ \mathbf{m}_{2+\omega} \cos(kz) - i\mathbf{m}_{1,0\omega}) + (\hbar/e)\tau_D (ic_+ \mathbf{m}_{2+\omega} \cos(kz) - i\mathbf{m}_{1,0\omega}) - J(-c_+ \mathbf{m}_{2+} \cos(kz) + \mathbf{m}_{1,0}) \right]. \quad (\text{S9.17})$$

From the multiplication of \mathbf{m}_{2-}^* we obtain:

$$\begin{aligned}
0 = \mathbf{m}_{2-}^* & \left[-2Ac_- \kappa \mathbf{m}_{2-} \sin(\kappa z) \right. \\
& - (\hbar/e) \tau_F \hat{\mathbf{y}} \times (ic_- \mathbf{m}_{2-} \omega \cos(\kappa z) + ic_+ \mathbf{m}_{2+} \omega \cos(\kappa z) - i\mathbf{m}_{1,0} \omega) \\
& + (\hbar/e) \tau_D (ic_- \mathbf{m}_{2-} \omega \cos(\kappa z) - i\mathbf{m}_{1,0} \omega) \\
& \left. - J(-c_- \mathbf{m}_{2-} \cos(\kappa z) + \mathbf{m}_{1,0}) \right]. \tag{S9.18}
\end{aligned}$$

We now can solve the system of equations consisting of Eq. (S9.17) and Eq. (S9.18) to obtain the complex coefficients c_{\pm} as a function of the four variables $\mathbf{m}_1(\hat{\mathbf{y}} \times \mathbf{m}_{2\pm})$ and $\mathbf{m}_{2\mp}(\hat{\mathbf{y}} \times \mathbf{m}_{2\pm})$:

$$\begin{aligned}
c_{\pm} = \frac{\pm 1}{c} & \left[2A\kappa \sin(d\kappa) (J\mathbf{m}_{1,0}(\hat{\mathbf{y}} \times \mathbf{m}_{2\mp}) - i(\hbar/e)\omega(\mathbf{m}_{1,0}\mathbf{m}_{2\mp}\tau_F + \mathbf{m}_{1,0}(\hat{\mathbf{y}} \times \mathbf{m}_{2\mp})\tau_D)) \right. \\
& \left. + \mathbf{m}_{1,0}(\hat{\mathbf{y}} \times \mathbf{m}_{2\mp}) \cos(d\kappa) \left((\hbar/e)^2 \omega^2 (\tau_D^2 + \tau_F^2) + 2i(\hbar/e)J\tau_D\omega - J^2 \right) \right] \tag{S9.19}
\end{aligned}$$

where the prefactor c is given by:

$$\begin{aligned}
c = \cos(d\kappa) & \left[2A\kappa \sin(d\kappa) (J\mathbf{m}_{2+}(\hat{\mathbf{y}} \times \mathbf{m}_{2-}) + i(\hbar/e)\omega(\mathbf{m}_{2-}(\hat{\mathbf{y}} \times \mathbf{m}_{2+})\tau_D - \mathbf{m}_{2-}\mathbf{m}_{2+}\tau_F)) \right. \\
& \left. + \mathbf{m}_{2+}(\hat{\mathbf{y}} \times \mathbf{m}_{2-}) \cos(d\kappa) \left((\hbar/e)^2 \omega^2 (\tau_D^2 + \tau_F^2) + 2i(\hbar/e)J\tau_D\omega - J^2 \right) \right] \\
& + 2Ak \sin(dk) \left[-2A\kappa \mathbf{m}_{2+}(\hat{\mathbf{y}} \times \mathbf{m}_{2-}) \sin(d\kappa) + \cos(d\kappa) (J\mathbf{m}_{2+}(\hat{\mathbf{y}} \times \mathbf{m}_{2-}) \right. \\
& \left. + i(\hbar/e)\omega(\mathbf{m}_{2-}\mathbf{m}_{2+}\tau_F + \mathbf{m}_{2-}(\hat{\mathbf{y}} \times \mathbf{m}_{2+})\tau_D)) \right]. \tag{S9.20}
\end{aligned}$$

The complex coefficients c_{\pm} now specify the YIG solution and contain the influence of the Co layer. Using the eigenvectors Eq. (S9.11) and Eq. (S9.10) together with the wavevectors Eq. (S9.6) and Eq. (S9.7) and the complex coefficients Eq. (S9.20) and Eq. (S9.19) in the ansatz Eq. (S9.14) yields the spatially-dependent YIG magnetization. Using subsequently the ansatz Eq. (S9.14) and Eq. (S9.15) in the modified LLG Eq. (S9.2) allows to extract the Co susceptibility $\tilde{\chi}_1$ by sorting the resulting expression by the transverse Co magnetization components $(m_{1,z}, m_{1,x})$. We find

$$\tilde{\chi}_1^{-1} = \begin{pmatrix} \chi_{1,zz}^{-1} & \chi_{1,xz}^{-1} \\ \chi_{1,zx}^{-1} & \chi_{1,xx}^{-1} \end{pmatrix} \iff \tilde{\chi}_1 = \frac{1}{\chi_{1,zz}^{-1}\chi_{1,xx}^{-1} - \chi_{1,zx}^{-1}\chi_{1,xz}^{-1}} \begin{pmatrix} \chi_{1,xx}^{-1} & -\chi_{1,zx}^{-1} \\ -\chi_{1,zx}^{-1} & \chi_{1,zz}^{-1} \end{pmatrix} \tag{S9.21}$$

where the entries of the inverse susceptibility are:

$$\chi_{1,zz}^{-1} = \frac{i\alpha_1\omega}{\gamma_1} + \mathbf{m}_2(d_2) \frac{-i(\hbar/e)\tau_D\omega + i(\hbar/e)\tau_F\omega + J}{d_1 M_{s,1}} + \frac{i(\hbar/e)\tau_D\omega - J}{d_1 M_{s,1}} - \mu_0(H + M_{s,1}), \tag{S9.22}$$

$$\chi_{1,zx}^{-1} = -\frac{i\omega}{\gamma_1} + \mathbf{m}_2(d_2) \frac{-i(\hbar/e)\tau_D\omega + i(\hbar/e)\tau_F\omega + J}{d_1 M_{s,1}} - \frac{i(\hbar/e)\tau_F\omega}{d_1 M_{s,1}}, \tag{S9.23}$$

$$\chi_{1,xz}^{-1} = \frac{i\omega}{\gamma_1} + \mathbf{m}_2(d_2) \frac{-i(\hbar/e)\tau_D\omega - i(\hbar/e)\tau_F\omega + J}{d_1 M_{s,1}} + \frac{i(\hbar/e)\tau_F\omega}{d_1 M_{s,1}}, \tag{S9.24}$$

$$\chi_{1,xx}^{-1} = \frac{i\alpha_1\omega}{\gamma_1} + \mathbf{m}_2(d_2) \frac{-i(\hbar/e)\tau_D\omega - i(\hbar/e)\tau_F\omega + J}{d_1 M_{s,1}} + \frac{i(\hbar/e)\tau_D\omega - J}{d_1 M_{s,1}} - \mu_0 H. \tag{S9.25}$$

However, an analytical solution of the resonance condition $\det \tilde{\chi}_1^{-1} = 0$ is not possible. A numerical solution has been used to compute the results presented in the main

text using

$$\chi_{1,xx} = \frac{\chi_{1,zz}^{-1}}{\chi_{1,zz}^{-1}\chi_{1,xx}^{-1} - \chi_{1,zx}^{-1}\chi_{1,xz}^{-1}}. \tag{S9.26}$$

Note that we can obtain analytical resonance conditions in the macrospin approximation. For this we have to

replace the spatially-dependent YIG magnetization by an uniform magnetization $\mathbf{m}_2(d_2) \rightarrow \mathbf{m}_2$ in Eq. (S9.2).

S10. SIMULATION OF THE EXCHANGE MODE

Fig. S10(a) shows the color map for a pure antiferromagnetic exchange coupling between the YIG and Co layers. We find an exchange mode at higher frequencies than the Co resonance and symmetric avoided crossings.

In Fig. S10(b) we show the color map for a field-like torque which is substantially smaller than the damping-like torque. We observe a dominant mode-locking of the YIG and Co resonances. In metallic systems [?] we expect that the torques are primarily damping-like, as the real part of the spin mixing conductance exceeds the imaginary part. However, for insulating interfaces the amplitudes of the torques are less clear. Here, we find that our experiments are not reproduced with a dominant damping-like torque.

In Fig. S10(c) we plot the color map for $\tau_F = -30 \text{ A s/m}^2$, $\tau_D = 15 \text{ A s/m}^2$ and $J = 0$. Note that this configuration refers to the situation of the YIG/Cu(5)/Co(50) sample from Fig. 1(b),(e) with an inverted field-like torque. We find that the intensity symmetry of the avoided crossings is now also inverted compared to the experimental data (inset). Therefore, we know the sign of the field-like torque is positive for the YIG/Cu(5)/Co(50) samples.

In Fig. S10(d) we show the color map for the YIG/Co(50) sample for a positive field-like torque and a strong antiferromagnetic coupling. The avoided crossings are symmetric, as the influence of the field-like torque is much smaller than the exchange torque. When we compare Fig. S6(b), Fig. 3(a), and Fig. S10(d), we find that all used parameter combinations produce avoided crossings, with slightly different intensity modifications in the dispersion branches of the coupled systems. Due to the similar effects of the exchange torques and field-like torques, it is challenging to determine the signs of these torques for the YIG/Co samples without an interlayer.

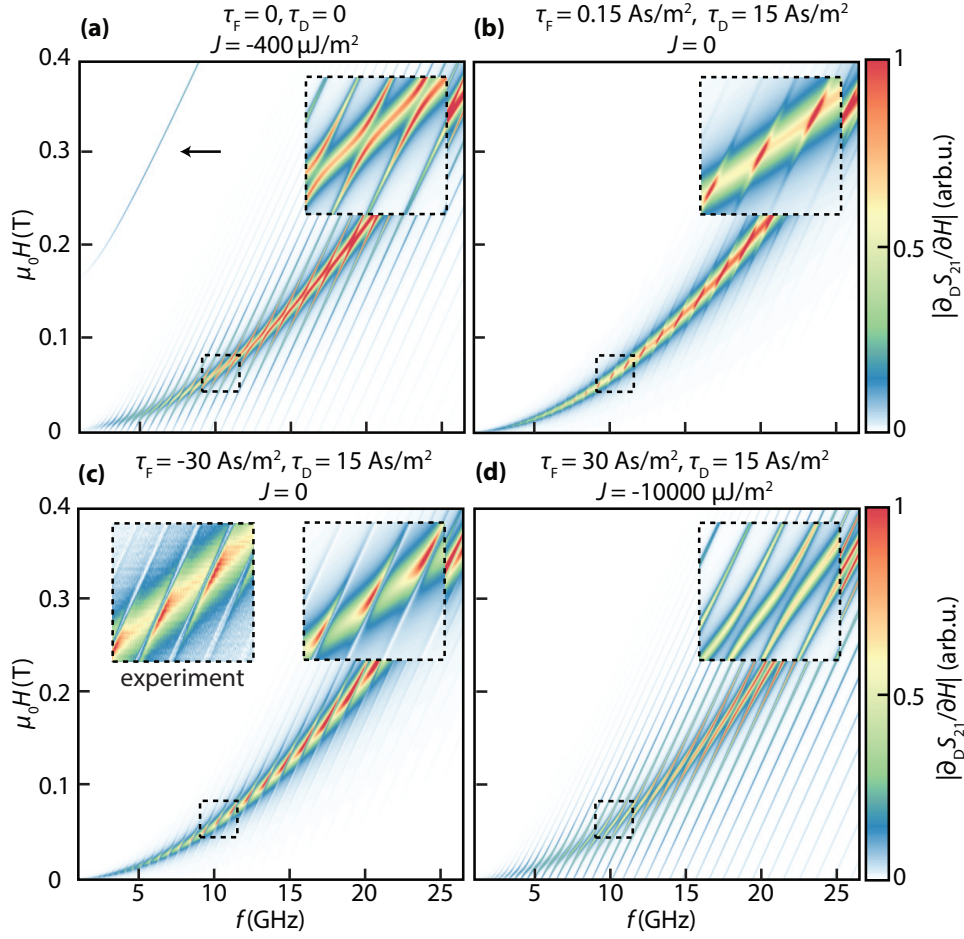


FIG. S10. (a) An exchange coupling can reproduce the exchange mode in the experiment. (b) A dominant damping-like torque results in a mode-locking of the YIG and Co resonances. (c) The sign of the field-like torques determines the asymmetry of the color code. We require a positive field-like torque to simulate the YIG/Cu(5)/Co(50) experiments, cf. Fig. 3 (b). (d) A dominant antiferromagnetic exchange torque produces symmetric avoided crossings.

-
- S. Pütter, S. Geprägs, R. Schlitz, M. Althammer, A. Erb, R. Gross, and S. T. B. Goennenwein, *Applied Physics Letters* **110**, 012403 (2017).
- H. Maier-Flaig, S. T. B. Goennenwein, R. Ohshima, M. Shiraishi, R. Gross, H. Huebl, and M. Weiler, (2017), [arXiv:1705.05694](https://arxiv.org/abs/1705.05694).
- M. A. W. Schoen, J. M. Shaw, H. T. Nembach, M. Weiler, and T. J. Silva, *Physical Review B* **92**, 184417 (2015).
- A. J. Berger, E. R. J. Edwards, H. T. Nembach, J. M. Shaw, A. D. Karenowska, M. Weiler, and T. J. Silva, *Physical Review B* **97**, 094407 (2018).
- H. Maier-Flaig, M. Harder, R. Gross, H. Huebl, and S. T. B. Goennenwein, *Physical Review B* **94**, 054433 (2016).
- S. Klingler, A. V. Chumak, T. Mewes, B. Khodadadi, C. Mewes, C. Dubs, O. Surzhenko, B. Hillebrands, and A. Conca, *Journal of Physics D: Applied Physics* **48**, 015001 (2015).
- C. Dubs, O. Surzhenko, R. Linke, A. Danilewsky, U. Brückner, and J. Dellith, *Journal of Physics D: Applied Physics* **50**, 204005 (2017).
- G. Carlotti, G. Gubbiotti, L. Pareti, G. Socino, and G. Turilli, *Journal of Magnetism and Magnetic Materials* **165**, 424 (1997).
- P. Hansen, P. Röschmann, and W. Tolksdorf, *Journal of Applied Physics* **45**, 2728 (1974).
- A. G. Gurevich and A. N. Anisimov, *Sov Phys JETP* **41**, 336 (1975).
- P. F. Herskind, A. Dantan, J. P. Marler, M. Albert, and M. Drewsen, *Nature Physics* **5**, 494 (2009).
- P. Landeros and D. L. Mills, *Physical Review B* **85**, 054424 (2012).
- M. Körner, K. Lenz, R. A. Gallardo, M. Fritzsche, A. Mücklich, S. Facsko, J. Lindner, P. Landeros, and J. Fassbender, *Physical Review B* **88**, 054405 (2013).
- M. Krawczyk, S. Mamica, M. Mruczkiewicz, J. W. Klos, S. Tacchi, M. Madami, G. Gubbiotti, G. Duerr, and D. Grundler, *Journal of Physics D: Applied Physics* **46**, 495003 (2013).
- R. A. Gallardo, A. Banholzer, K. Wagner, M. Körner, K. Lenz, M. Farle, J. Lindner, J. Fassbender, and P. Landeros, *New Journal of Physics* **16**, 023015 (2014).
- R. McMichael and P. Krivosik, *IEEE Transactions on Magnetics* **40**, 2 (2004).
- R. Arias and D. L. Mills, *Physical Review B* **60**, 7395 (1999).
- R. D. McMichael, *Journal of Applied Physics* **103**, 07B114 (2008).
- S. S. Kalarickal, P. Krivosik, M. Wu, C. E. Patton, M. L. Schneider, P. Kabos, T. J. Silva, and J. P. Nibarger, *Journal of Applied Physics* **99**, 093909 (2006).
- M. Vohl, J. Barnaś, and P. Grünberg, *Physical Review B* **39**, 12003 (1989).
- J. Xiao and G. E. W. Bauer, *Physical Review Letters* **108**, 217204 (2012).
- G. Rado and J. Weertman, *Journal of Physics and Chemistry of Solids* **11**, 315 (1959).
- B. Heinrich, Y. Tserkovnyak, G. Woltersdorf, A. Brataas, R. Urban, and G. E. W. Bauer, *Physical Review Letters* **90**, 187601 (2003).